POLITECNICO DI TORINO
Repository ISTITUZIONALE

A modelling and experimental study on the co-precipitation of Ni0.8Mn0.1Co0.1(OH)2 as precursor for battery cathodes

(Article begins on next page)
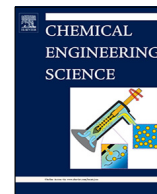
08 September 2024

A modelling and experimental study on the co-precipitation of Ni$_{0.8}$Mn$_{0.1}$Co$_{0.1}$(OH)$_2$ as precursor for battery cathodes

Maria Laura Para, Mojtaba Alidoost, Mohsen Shiea, Gianluca Boccardo, Antonio Buffo, Antonello A. Barresi, Daniele Marchisio *

Department of Applied Science and Technology (DISAT), Institute of Chemical Engineering, Politecnico di Torino, Torino, Italy

HIGHLIGHTS

- Coprecipitation of Ni$_{0.8}$Mn$_{0.1}$Co$_{0.1}$(OH)$_2$ from soluble metal salts is investigated.
- Mixing is controlled via a Multi-Inlet Vortex Mixer (MIVM).
- Nucleation, growth and agglomeration are identified as key phenomena.
- A population balance model is developed to simulate the coprecipitation process.
- Coprecipitation conditions affect particle morphology, crystallinity & size distribution.

ARTICLE INFO

ABSTRACT

A multi-inlet vortex mixer is used to investigate the co-precipitation of Ni$_{0.8}$Mn$_{0.1}$Co$_{0.1}$(OH)$_2$ particles, largely employed to produce Li-ion battery cathodes. The co-precipitation process is simulated with a population balance model, adopted to describe the experimental findings and gain deeper understanding of the process. Experiments and simulations are carried out under different operating conditions to quantify the effect of mixing conditions, turbulence and feed reactant concentrations on the final characteristics of the obtained particles, such as the size distribution, structure, morphology and density. These characteristics are measured by conducting static light-scattering, FESEM and XRD analyses and are expected to have, in turn, a tremendous effect on the final electrochemical performance of the cathode. Based on the experimental and modelling observations, we discuss the role of nucleation, molecular growth and aggregation in the co–precipitation process. Eventually a possible mechanism explaining the formation of Ni$_{0.8}$Mn$_{0.1}$Co$_{0.1}$(OH)$_2$ particles is proposed.

1. Introduction

Lithium-ion batteries are growing exponentially in diverse applications, such as electric portable devices and appliances, electric vehicles and stationary energy storage systems, due to their versatility and high energy density. This growth has been driving a considerable amount of research toward developing batteries of desired characteristics, e.g., larger capacity, higher energy density, longer lifetime, greater safety and lower environmental impact. It is well-known that these decisive characteristics are also determined by the cathode properties, which in turn are inherited from the cathode's precursor material. In this regard, layered nickel-manganese-cobalt based materials are one of the most interesting cathodes for lithium-ion batteries, due to their high capacity and structural and thermal stability. The precursor material of these cathodes is nickel-manganese-cobalt hydroxide, Ni$_{1-x-y}$Mn$_x$Co$_y$(OH)$_2$, which is produced via a co-precipitation typically conducted in continuous stirred tank reactors (CSTR).

A better understanding of the co-precipitation process and the development of a predictive mathematical model for its simulation can play an important role in process scale-up, design and optimization, and can help meeting the increasing demand for these materials. Indeed, it is fundamental to understand the effect of the operating conditions on the final particle properties, such as the mean particle size, broadness of the size distribution and particle tap density. For instance, Lee and co-workers (Lee et al., 2004) studied the production of Ni$_{1/3}$Mn$_{1/3}$Co$_{1/3}$(OH)$_2$ in the presence of ammonia (as chelating agent) by using a CSTR operating under

* Corresponding author at: Dipartimento di Scienza Applicata eTecnologia, Politecnico di Torino, Corso Duca degli Abruzzi 24, 10129 Torino, Italy.
E-mail address: daniele.marchisio@polito.it (D. Marchisio).

inert nitrogen atmosphere. They stated that the most influential factors on the final particle properties are the pH, chelating agent concentration and stirring rate. In another example, Van Bommel and Dahn (van Bommel & Dahn, 2009) studied the co-precipitation of nickel, manganese and cobalt-containing hydroxides in a CSTR and concluded that the dissolution/recrystallization of particles in the presence of ammonia results in the growth of spherical particles.

However, the literature review reveals that the co-precipitation of $Ni_{1-x-y}Mn_xCo_y(OH)_2$ has been mainly studied in CSTRs with long residence times, i.e., several hours. In contrast, little attention has been paid to the early-stage formation of particles in the co-precipitation of $Ni_{1-x-y}Mn_xCo_y(OH)_2$, which is indeed important to broaden our knowledge about such a process. For instance, the nucleation of particles occurs in a very short time after the mixing of the reactants and deserves investigations. Such knowledge paves the way for a successful scale-up and optimization of the co-precipitation process and enables us to develop reliable computational models.

In this work, we study the co-precipitation of $Ni_{0.8}Mn_{0.1}Co_{0.1}(OH)_2$ in its early stages by using a multi-inlet vortex mixer (MIVM). This setup has been successfully used to study fast reactive processes, such as precipitation, in which mixing is an important factor (Bensaid et al., 2014; Cheng & Fox, 2010; Ferri et al., 2017; Lince et al., 2011; Liu et al., 2008; Marchisio et al., 2008). In addition, a computational model is developed, fitted and validated to simulate the formation of particles and their subsequent evolution. The model provides further insight into the experimental observations and can be profitably used to design, optimize and scale-up these co-precipitation processes. Measurements and model predictions allow us to discuss the interplay between nucleation, molecular growth and aggregation in determining the final particle characteristics.

2. Experimental details and operating conditions

2.1. Co-precipitation of $Ni_{0.8}Mn_{0.1}Co_{0.1}(OH)_2$

$Ni_{0.8}Mn_{0.1}Co_{0.1}(OH)_2$, also known as NMC811 hydroxide, is synthesized by mixing aqueous solutions of metal sulfates (MSO_4 with M = Ni, Co, Mn), NaOH and NH_3 in a MIVM shown in Fig. 1. The feeds enter from four inlets with the same flow rate. The solutions of MSO_4 and NH_3 are injected from two opposite inlets, while the solution of NaOH enters from the other two. The aqueous feed solutions of NaOH, NH_3 and MSO_4 are prepared with de-aerated milliQ (obtained by boiling water for 10 min). All the solutions are bubbled for 60 min with nitrogen before each experiment. Two syringe pumps (KDScientific-100) are used to control the solution feeding, which are connected by polypropylene pipes to the four inlets. The metal feed concentration, $[M^{2+}]$, is varied from 0.01 to 2 M, keeping the molar ratio between Ni^{2+}, Mn^{2+} and Co^{2+} ions fixed at 8:1:1. The concentration of NaOH feed solution is equal to that of the metal feed solution, but as NaOH enters from two inlets, the initial concentration ratio between MSO_4 and NaOH of the mixed feeds, $[M^{2+}]:[NaOH]$, is always 1:2. Moreover, different total flow rates (sum of the four inlet flow rates) of 33, 70, 105 and 169 mL/min are tested. All the experimental conditions are repeated five times for three ratios between the metal and NH_3 feed concentrations, i.e., $[M^{2+}]:[NH_3]$ = 1:0.5, 1:1, 1:2. In what follows, the different experiments are labelled with the metal feed concentration, total flow rate and the initial concentration ratio between MSO_4 and NH_3 of the mixed feeds, i.e., $[M^{2+}]:[NH_3]$. Table 1 summarizes the experimental conditions studied in this work. The suspension of particles is collected at the outlet of the MIVM to perform the characterizations. For the particle size
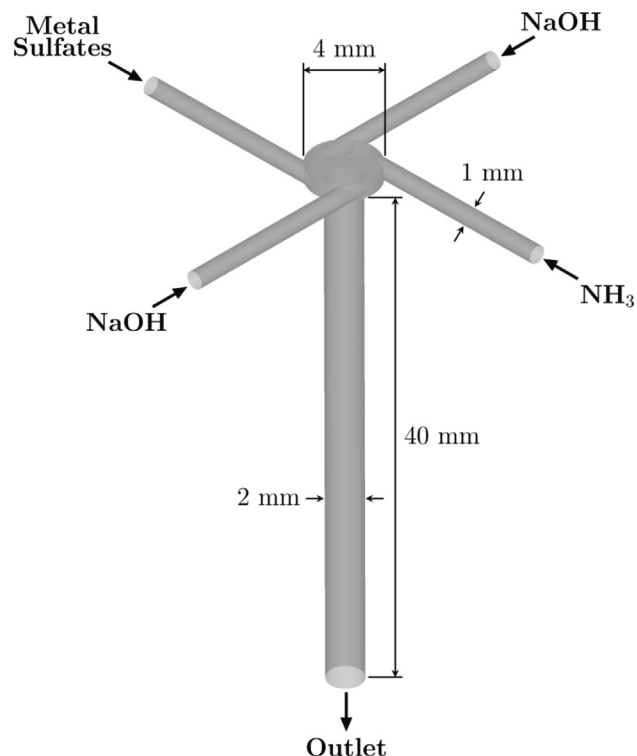
distribution (PSD) measurements, an aliquot is quenched immediately by dilution in water to cease the co-precipitation process, while some suspension drops are deposited on a filter paper to prepare the sample for the FESEM characterization. The dilution ratio ranges from 0 to 1/200 depending on the concentration of the feed solution, and it is set in such a way to obtain the highest dilution that allows the PSD measurement. Finally, the remaining suspension is filtrated by using Whattman grade 40 filter paper, and then rinsed by purring abundant milliQ water (18.2 MΩ cm resistivity) until neutral pH. Finally, it is left drying at room temperature in open air. The dried mixed metal hydroxide is mortared to obtain a fine dust for XRD characterizations and tap density measurements.

2.2. Particle characterization

Several characterizations are performed to obtain information about the precipitated particles, including particle morphology, crystallite size, primary and secondary particle size and tap density. It is indeed informative to observe the effect of synthesis conditions on these properties and then link the observations with the relevant particulate processes involved, namely nucleation, molecular growth and aggregation. It is noteworthy that these particle characteristics play an important role in determining the final electrochemical performance of batteries (Barai et al., 2019; Zhou et al., 2010).

As it will become clearer later, particles are formed by large aggregates of smaller particles. These large aggregates will be referred to as secondary particles, whereas their building blocks will be referred to as primary particles. Morphological characterization is performed by a Field-Emission Scanning Electron Microscopy (FESEM, ZEISS Supra 40) which allows to observe more closely primary particles. The precipitate sample is prepared by placing some drops of the fluid sample on a filter paper and letting them dry at room temperature followed by metallization with

Fig. 1. The schematic diagram of the multi-inlet vortex mixer (MIVM).

Table 1
Experimental conditions.

Total flow rate (mL/min)	Residence time (ms)	Metal feed concentration (mol/L)							
		0.01	0.02	0.04	0.1	0.2	0.4	1	2
33	257	X						X	
70	121	X	X	X	X	X	X	X	X
105	81	X						X	
169	50	X	*		X	*		X	*

[(X)] Experiments performed for all three $[M^{2+}]$:$[NH_3]$ ratios of "1:0.5″,"1:1″,"1:2″.
[(*)] Experiments performed only for $[M^{2+}]$:$[NH_3]$ ratio of "1:1″.

chromium. Several images are taken from different parts of the sample; these images allow us to analyze the structure of the particles both qualitatively and quantitatively.

The particle size distribution (PSD) is determined by the static light-scattering equipment Beckman Coulter LS 230. The device prevents particle sedimentation by mechanical circulation of the sample. An optical small module is used, and the scattered pattern of light is analyzed with the Fraunhofer optical model, considering the refractive index of water (RI: 1.333). The refractive index of particles is not exactly known, but nickel hydroxide has a refractive index of 1.82–1.88. However, the particles are opaque with a size (>20 μm) larger than wavelength of the light, and therefore, the Fraunhofer model is adequate to calculate their size, in which the refractive index of the solid can be neglected. Measurement acquisition time is 60 s. Due to the nature of this measurement, it is assumed that the observed PSD is that of the secondary particles.

X-Ray diffraction (XRD) patterns of mortared powder samples are collected by using a PANalytical X'Pert PRO (Cu Kalfa radiation, λ = 0.154187 nm) diffractometer, with a 2D solid PIXcel detector, a solid-state detector with rapid readout time and high dynamic range. The diffractograms were obtained in the 2θ range from 10 to 80°, with a step size of 0.026° (2 θ), at 40 kV and 40 mA. The diffractograms are employed to identify crystal phases of the precipitate and, in addition, to calculate the crystallite size by the Scherrer method.

Tap density is determined by filling a glass capillary with a known amount of mortared sample, followed by tapping until no further volume change is detected.

Experiments and characterization measurements are repeated to assess the reproducibility and uncertainty whenever possible. The uncertainties are graphically represented in the figures by error bars with the length of one standard deviation, and therefore, they correspond to a confidence interval of approximately 68%.

2.3. Co-precipitation model

A simplified model, based on the population balance equation (PBE), is adopted to simulate the co-precipitation in the MIVM as a plug flow reactor. With this assumption, the governing equations can be simplified to ordinary differential equations. For modelling, the process is divided into several sub-steps as follows. The supersaturation, as the driving force of the co-precipitation process, is generated by the turbulent mixing of the reactants, whose effect is considered by employing a micromixing model. Then, the generated supersaturation induces the formation of particles by nucleation and molecular growth. Particles can also undergo aggregation to form larger particles. The formation and evolution of particles by nucleation, molecular growth and aggregation is described by the PBE. Simultaneously, the consumption of reactant species is described by coupling the species mass balance equations with the PBE. In the following sections, the main elements of the modelling framework are detailed.

2.4. Micromixing model

In this work, molecular mixing or micromixing is considered by employing a multi-environment model, in which the distribution of composition is described by defining some environments that exchange mass due to mixing (Fox, 1998; Marchisio et al., 2002). In this model, at a given time and spatial position, each environment has a certain probability (or volume fraction) and certain local species concentrations. Here, we adopt the simplest arrangement that consists of four environments, three of which are associated to three feed solutions, i.e., metal, sodium hydroxide and ammonia feeds, that mix to form the (fourth) co-precipitation environment. Thus, it is assumed that the reaction occurs only in the co-precipitation environment. In this model, the probability of the feed environments decreases by micromixing, which results in the increase of the co-precipitation environment probability or volume fraction. Moreover, the concentration of feed environments is assumed to be constant and equal to that at the inlets. The probability of the feed environments is evolved according to the following equation (Fox, 1998):

$$\frac{dp_i}{dt} = -r_i \quad \text{for} \quad i \in \{1,2,3\}, \tag{1}$$

where p_i is the volume fraction of environment i and r_i is the probability flux from the feed environment i to the precipitation environment due to micromixing. The probability of the precipitation environment (p_4) is calculated instead of being tracked, since the probabilities sum to unity. The following expression is used for the probability fluxes (Fox, 1998):

$$r_i = \gamma p_i(1 - p_i) \quad \text{for} \quad i \in \{1,2,3\}, \tag{2}$$

here γ determines the micromixing rate, which depends on the local turbulence, and is usually described in terms of the turbulent kinetic energy (k) and dissipation rate (ε). In this work, it is modelled as follows (Marchisio et al., 2001):

$$\gamma = C_f \frac{C_\phi}{2} \frac{\varepsilon}{k} \quad \text{for} \quad i \in \{1,2,3\}, \tag{3}$$

where C_f and C_ϕ are coefficients of the model. In the case of high Reynolds number, C_ϕ is set to 2. However, Liu and Fox (Liu & Fox, 2006) argued that this value leads to the overestimation of micromixing rate in the case of liquids, and they proposed a correlation for C_ϕ that takes into account the local turbulent Reynolds number ($Re_l = \frac{k}{\sqrt{\varepsilon\nu}}$):

$$C_\phi = \sum_{n=1}^{6} a_n (\log_{10} Re_l)^n. \tag{4}$$

The coefficients a_n are reported in the work of Liu and Fox (Liu & Fox, 2006).

In Eq. (3), C_f is introduced as a correction coefficient to match the scalar dissipation rate predicted by the multi-environment model and that calculated for turbulent flows under the assumption of fully developed scalar spectrum (Marchisio et al., 2001). Moreover, the local Reynolds number depends on the turbulent

kinetic energy and dissipation rate, the profiles of which are extracted from computational fluid dynamics (CFD) simulations of the micromixer. These profiles and the procedure to obtain them are reported in the Supplementary Material. It should be mentioned that the turbulence data (obtained from the CFD simulation) is available until the residence time of the micromixer. After that time, no turbulence is assumed in the modelling. However, this has no effect on the micromixing, as the complete mixing is achieved rapidly before the solution exits the micromixer.

2.5. Population balance model

The evolution of the particulate system is described in terms of the PSD that is governed by the population balance equation (PBE). In this work, the PBE is solved by adopting the quadrature method of moments (QMOM) (Marchisio et al., 2003). In this approach, the PSD is approximated by an N-node quadrature that is the summation of N weighted Dirac delta functions, each located on an abscissa. The N weights and abscissas of the quadrature are calculated from a set of $2N$ moments of the PSD by employing an inversion algorithm. Therefore, it is required to track $2N$ (usually low order) moments of the PSD. The moment of order k is defined as follows:

$$m_k = \int_0^\infty L^k n(L) dL, \tag{5}$$

with L denoting the particle size. Since it is assumed that particle formation occurs in the precipitation environment, we define the volume-weighted moments in that environment as $\langle m_k^{(4)}\rangle = p_4 m_k^{(4)}$, for which the following governing equations can be written:

$$\frac{d\langle m_k^{(4)}\rangle}{dt} = p_4 h_k^{(4)}, \tag{6}$$

where $h_k^{(4)}$ represents the rate of change of the k-order moment due to nucleation, molecular growth and aggregation. The calculation of $h_k^{(4)}$ is found elsewhere (Marchisio et al., 2003). These phenomena depend on the local species concentrations in the precipitation environment, which can be determined from the volume-weighted total concentrations of that environment, $s_\alpha^{(4)} = p_4 c_{T,\alpha}^{(4)}$, for nickel, manganese, cobalt, ammonia, sodium and sulfate. These concentrations are found by solving the following governing equations simultaneously with the moment equations:

$$\frac{ds_\alpha^{(4)}}{dt} = \sum_{i=1}^3 r_i c_{T,\alpha}^{(i)} + p_4 Q_\alpha^{(4)}, \tag{7}$$

The first term on the right-hand side of Eq. (7) describes the mass exchange due to micromixing, where $c_{T,\alpha}^{(i)}$ denotes the total concentration of species α in environment i, and it is constant for pure environments. Moreover $Q_a^{(4)}$ represents the consumption rate of the reactants involved in the co-precipitation, i.e., nickel, manganese and cobalt. It is calculated from the change in the total volume of the particles, that is $h_3^{(4)}$, by assuming that particles have spherical shape. The assumption of spherical shape for particles is a simplification made in the model due to the lack of information about the shape of particles.

Now, we turn our attention to the models used for nucleation, molecular growth, and aggregation. Their rates depend on supersaturation (S) which is defined as (Mersmann, 2001):

$$S = \sqrt[3]{\frac{\left(a_{Ni^{2+}}\right)^{0.8}\left(a_{Mn^{2+}}\right)^{0.1}\left(a_{Co^{2+}}\right)^{0.1}\left(a_{OH^-}\right)^2}{\left(k_{sp}^{Ni(OH)_2}\right)^{0.8}\left(k_{sp}^{Mn(OH)_2}\right)^{0.1}\left(k_{sp}^{Co(OH)_2}\right)^{0.1}}}. \tag{8}$$

In Eq. (8), activity of species and solubility product of metal hydroxides are denoted by a and k_{sp}, respectively. It is noteworthy that the formulation of the supersaturation in Eq. (8) assumes that the metal composition of particles is the same as that of the liquid, which is supported by some reports in the literature (Kosova et al., 2007). The activities needed in Eq. (8) are calculated by solving chemical equilibria of reactions, excluding that of the co-precipitation. The calculation steps are detailed below. In the calculation of supersaturation, the activity product of each metal hydroxide, $M(OH)_2$, in Eq. (8) is arranged as: $a_{M^{2+}}(a_{OH^-})^2 = \left[M^{2+}\right][OH^-]^2\gamma_\pm^3$, where, $\gamma_\pm$ denotes the mean molal activity coefficient, and it is estimated for each pair of the cation metal and hydroxide ion by employing the Bromley's method (Bromley, 1973) adapted for multi-component solutions. Moreover, the effect of ammonia on the activity coefficients is neglected. It is noteworthy that the validity of this method is limited to solutions with ionic strengths below 6 M, which is the case of the experimental conditions explored in this work. The coefficients used in the Bromley's model are reported in the Supplementary Material.

For the nucleation model, we adopt the following expression that consists of two contributions for homogeneous and heterogeneous nucleation. The formulation of each contribution is based on the classical nucleation theory (Volmer & Weber, 1926):

$$J(S) = k_1 \exp\left(\frac{-B_1}{(\ln S)^2}\right) + k_2 \exp\left(\frac{-B_2}{(\ln S)^2}\right), \tag{9}$$

where k_1, B_1, k_2, B_2 are the modelling coefficients. It should be noted that the homogeneous nucleation is dominant at high supersaturation conditions and no presence of seed particles. Then, as the supersaturation decreases, the heterogeneous nucleation becomes the dominant mechanism. This behavior can be ensured by setting the following constraints in the parameter optimization: $k_1 > k_2$ and $B_1 > B_2$ (assuming the first term on the right-hand side of Eq. (9) is related to the homogeneous nucleation).

The molecular growth rate is modelled by the following size-independent expression:

$$G = k_G(S - 1). \tag{10}$$

Here, k_G is a modelling coefficient. The above model is selected since the parameter optimization usually failed when a size-dependent model was employed.

Brownian motions and turbulent fluctuations are considered as the underlying mechanisms for aggregation. The collision rate based on these two mechanisms are calculated, respectively, by (Mersmann & Braun, 2001; Saffman & Turner, 1956):

$$\beta_{ij}^{Br} = \frac{2k_BT}{3\mu}\frac{(L_i + L_j)^2}{L_iL_j}, \tag{11}$$

and by:

$$\beta_{ij}^{Turb} = 2.2943 C_T\sqrt{\frac{\varepsilon}{\nu}}(L_i + L_j)^3, \tag{12}$$

where L_i and L_j are the size of the colliding particles, k_B the Boltzmann constant, T the operating temperature, μ the fluid viscosity and C_T a correction coefficient accounting for deviations with respect to the simplification hypothesis employed while deriving Eq. (12). In addition, the following expression is used to estimate the aggregation efficiency (P_{ij}) under turbulent conditions (Bałdyga et al., 2003):

$$P_{ij} = \exp\left(-\frac{t_c}{t_i}\right), \tag{13}$$

here, $t_i = \sqrt{\nu/\varepsilon}$ estimates the interaction time of two colliding particles under turbulent conditions, while $t_c = [D_b/f(\delta)G]$ is the time needed for the formation of a stable bridge with diameter of D_b between two particles. Baldyga et al. (Bałdyga et al., 2003) suggested the following expression for the estimation of D_b:

$$D_\text{b} = \frac{\sqrt{\rho}(\varepsilon\nu)^{1/4}}{\sqrt{A_\text{p}}} \frac{L_i L_j}{\sqrt{L_i^2 + L_j^2 - L_i L_j}}, \qquad (14)$$

where, A_p represents the yield strength of the particles and ρ is the fluid density. Lastly, the shape function, $f(\delta)$, is calculated as follows (David et al., 1991):

$$f_\delta = \frac{4\left(1 + \delta - \sqrt{\delta^2 - 1}\right)}{\frac{1}{3} + \delta - \sqrt{\delta^2 - 1} - \left(\delta - \sqrt{\delta^2 - 1}\right)^2 \left(\frac{2\delta + \sqrt{\delta^2 - 1}}{3}\right)}, \qquad (15)$$

here, $\delta = L_i/L_j$ denotes the particle size ratio. It should be mentioned that the aggregation of particles is assumed to be active only in the micromixer (until the residence time of the micromixer, as shown in Table 1), for which the turbulence data is available from the CFD simulation of the micromixer. After that time, no aggregation is considered in the model.

The overall co-precipitation model contains seven unknown parameters: k_1, B_1, k_2, B_2, k_G, C_T, A_p. These are identified by fitting the experimental data via the optimization algorithm described in the Supplementary Material. It is noteworthy that we have attempted to avoid including the particle aggregation in the optimization, however, the aggregation of the particles was observed in all the experimental conditions investigated in this work, hence the necessity to include its effect in the modelling.

2.6. Chemical equilibria

The activity of the reactants are calculated by solving the chemical equilibria of the reactions shown in Table 2 (van Bommel & Dahn, 2009). By using the reaction constants and the relation between the corresponding reactants and products, the equilibrium calculations can be simplified to the solution of five non-linear equations written in terms of the equilibrium concentration of metal ions, ammonia and hydroxyl ion. These five equations are the mass balances on the total concentration of three metals and ammonia, and the electro-neutrality equation. They are solved by employing the Newton-Raphson method adapted for a system of non-linear equations (Isaacson & Keller, 1966). Moreover, the equilibrium calculation is simplified, by adopting some assumptions, to avoid the inclusion of activity coefficients. First, considering the basic operating condition (pH > 10), the contribution of water

self-ionization to the concentration of OH⁻ is negligible and, in addition, ammonia tends to exist undissociated. Therefore, it is assumed that the activity coefficients have little effect on the water self-ionization and ammonia dissociation. Furthermore, due to the lack of data for metal-ammonia complexes, it is assumed that the activity coefficient of the metal ions is the same as that of the metal-ammonia complexes since they have similar charges. However, it should be emphasized that the activity coefficients are included in the calculation of supersaturation. Lastly, it should be mentioned that the validation of the employed thermodynamic model is an insurmountable task due to the rapid change of the composition during the co-precipitation reaction. However, the measured pH at the equilibrium condition, i.e., end of the co-precipitation reaction, can be compared with the predicted one, which is shown in Figure S8 of the Supplementary Material for some of the investigated experimental conditions.

3. Results and discussion

Let us start by analyzing the typical predictions obtained by the model. Here, we direct our attention to the profiles of the supersaturation, pH, moments of the PSD and volume-averaged particle size, i.e., $d_{43} = m_4/m_3$. It is assumed here that the moments of the PSD and the corresponding volume-averaged, i.e., mean, particle size, refer to the secondary particles, experimentally characterized by static light-scattering. Fig. 2 shows the profiles of supersaturation and pH obtained for an experimental case with a
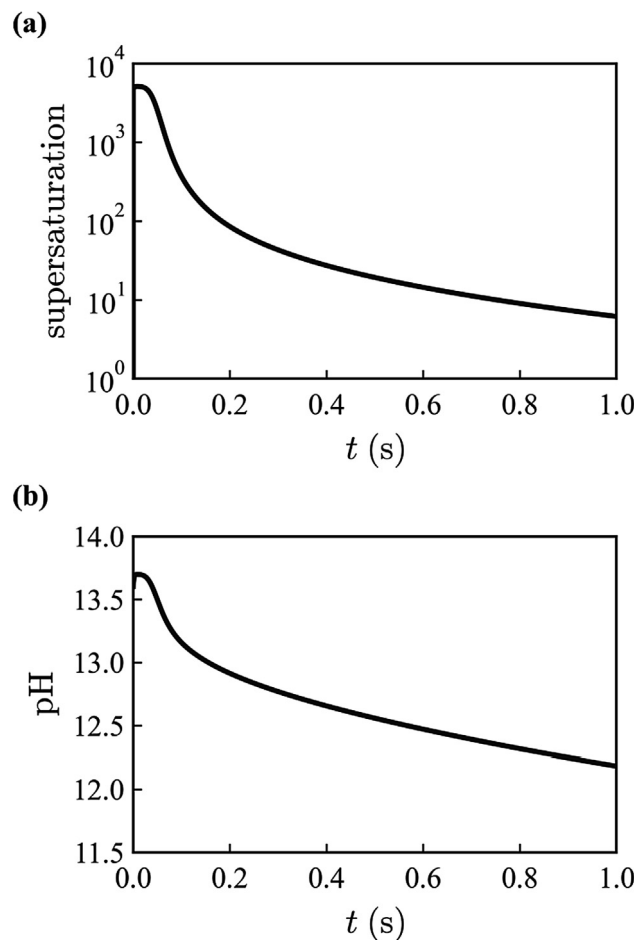
(a)

(b)

Fig. 2. Predicted profiles of supersaturation and pH vs time for experimental case with total flow rate of 70 mL/min, metal feed concentration of 1 M and $[M^{2+}]$:$[NH_3] = 1:1$.

Table 2

The equilibria of the Ni-Mn-Co hydroxide co-precipitation: $M_1^{2+} \equiv Ni^{2+}$, $M_2^{2+} \equiv Mn^{2+}$, $M_3^{2+} \equiv Co^{2+}$. The co-precipitation reaction, $M_i^{2+} + 2OH^- \leftrightarrow M_i(OH)_2$, is not included in the above equilibrium because the goal is to calculate the concentrations of the supersaturated solution.

Reactions	Log K		
	Ni	Mn	Co
$M_i^{2+} + NH_3 \leftrightarrow [M_i(NH_3)]^{2+}$	2.81	1.00	2.10
$M_i^{2+} + 2NH_3 \leftrightarrow [M_i(NH_3)_2]^{2+}$	5.08	1.54	3.67
$M_i^{2+} + 3NH_3 \leftrightarrow [M_i(NH_3)_3]^{2+}$	6.85	1.70	4.78
$M_i^{2+} + 4NH_3 \leftrightarrow [M_i(NH_3)_4]^{2+}$	8.12	1.3	5.53
$M_i^{2+} + 5NH_3 \leftrightarrow [M_i(NH_3)_5]^{2+}$	8.93	–	5.75
$M_i^{2+} + 6NH_3 \leftrightarrow [M_i(NH_3)_6]^{2+}$	9.08	–	5.14
$NH_3 + H_2O \leftrightarrow NH_4^+ + OH^-$	Log K_b = -4.80		
$H_2O \leftrightarrow H^+ + OH^-$	Log K_w = -14		

total flow rate of 70 mL/min, metal feed concentration of 1 M and concentration ratio $[M^{2+}]:[NH_3]$ equal to 1:1. Here, the predictions are shown until 1 (s), which is longer than the residence time of the micromixer. The reason is that the simulation by the model continues until the end of the co-precipitation that, in some conditions, may be achieved after the solution exits the micromixer. However, as mentioned previously, the aggregation is considered until the residence time of the micromixer, for which the turbulence data is available from the CFD simulation.

As can be seen in Fig. 2, the supersaturation decreases slowly in the first milliseconds, when small particles are nucleated. Then, the decrease accelerates due to the growth of many particles with significant size. Finally, the profile starts to get flat as the co-precipitation reaches the end. The same pattern is observed for pH, as hydroxyl ions are consumed during co-precipitation. The corresponding profiles for the moments of order 0 and 3, and the volume-averaged particle size ($d_{43} = m_4/m_3$) are shown in Fig. 3. The profile of m_0 confirms the first stage of intense nucleation of tiny particl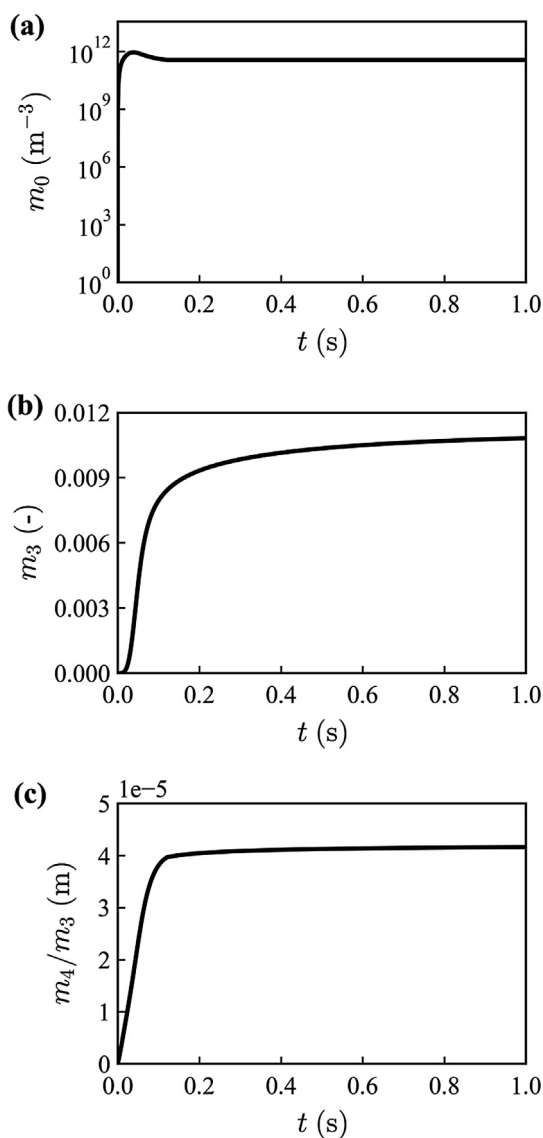es. The nucleated particles grow under supersaturated conditions and their total volume density increases, as can be seen from the profile of m_3. Moreover, the profile of m_0 shows that as the number of particles increases sufficiently, aggregation competes with the nucleation and, indeed, it can decrease the total number density of particles. Concerning d_{43}, the predictions show an increasing profile due to both molecular growth and aggregation.

Now we turn our attention to the experiments and the comparison with model predictions. Fig. 4 reports the mean particle size and span of the volume-weighted size distribution, measured by static light-scattering at different flow rates at the MIVM outlet, for a metal feed concentration of 1 M. Here, the mean size corresponds to the volume-averaged particle size, i.e., d_{43} of the PSD. Instead, the span characterizes the polydispersity of particles, and it is defined as $(d_{90} - d_{10})/d_{50}$ of the volume-weighted size distribution. In addition, the variability of the measurements between five repetitions of the experiments is shown on the plots by the error bars of a length equal to the standard deviation. Moreover, the model predictions are plotted on Fig. 4 for the purpose of comparison. It is worth to mention that span predictions are obtained by reconstructing the volume-weighted size distribution from the moments of the PSD. The details of the reconstruction are explained in the Supplementary Material. As can be seen from Fig. 4, the mean particle size decreases as the flow rate increases, for all the three different concentration ratios $[M^{2+}]:[NH_3]$ considered in this work. This can be associated to the effect of turbulence intensity on mixing and aggregation. In fact, a higher flow rate means more intense turbulent conditions, which increase the mixing rate. This can, in turn, generate higher supersaturation levels, hence boosting nucleation, which results in producing smaller particles. As far as aggregation is concerned, the increase of turbulence intensity has a dual effect. On one hand, it increases the collision rate between particles due to turbulent fluctuations, one the other hand, it reduces the probability with which the colliding particles aggregate. The overall effect can result in less aggregation of particles and, eventually, in the reduction of the mean size. Likewise, the span decreases with the increase of the flow rate. The sharpest difference of span is observed between the flow rate of 33 and 70 mL/min, corresponding to Reynolds numbers of 2820 and 4275 in the MIVM, respectively. This observation can be associated to the change of the flow regime, since the flow conditions in the case of the lowest flow rate cannot be identified as fully turbulent, in contrast to those in the case of the other investigated flow rates. In fact, no modelling attempt is made for the lowest experimental flow rate due to the difficulty in obtaining turbulence data from the CFD simulation of the micromixer operating at that flow rate.

The decreasing trend is observed also in the predictions for the mean size and span obtained by the simulation. In fact, a good agreement is achieved between the measurements and predictions of the mean size, which highlights the capability of the simplified approach to model the experimental setup. It should be noted that the modelling framework is used to simulate the MIVM under turbulent conditions, and therefore, the simulations are done for total flow rates down to 50 mL/min, corresponding to a Reynolds number of 4275 in the mixing chamber. Concerning the predicted span, despite the captured decreasing trend, a discrepancy is observed between the predicted and measured values. This discrepancy can be attributed to the plug flow assumption in the simplified model that can underestimate polydispersity. The polydispersity can be modelled more accurately by employing a coupled CFD-PBE approach (Shiea et al., 2020).

Furthermore, the model can be modified to assess the importance of aggregation. As it can be seen in Fig. 5, the predicted mean particle size remains virtually constant by removing aggregation from the model, and its absolute value is slightly lower than that
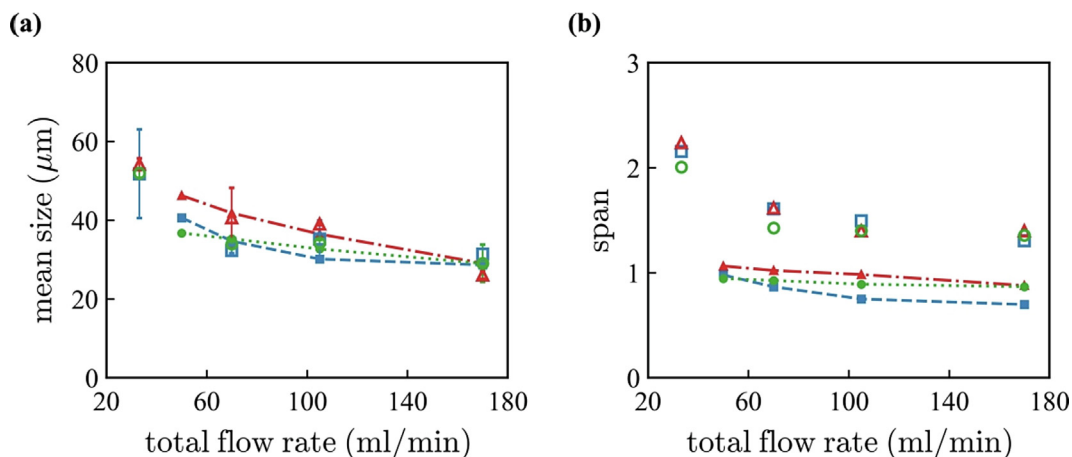

Fig. 3. Predicted profiles of m_0, m_3 and volume-averaged particle size vs time for experimental case with total flow rate of 70 mL/min, metal feed concentration of 1 M and $[M^{2+}]:[NH_3] = 1:1$.

(a)

(b)

Fig. 4. Measurements (hollow markers) and predictions (lines with filled markers) for the mean secondary particle size and span versus the flow rate for $[M^{2+}]:[NH_3]$ = "1:0.5" (green circles), "1:1" (red triangles) and "1:2" (blue squares). The metal feed concentration $[M^{2+}]$ is 1 M.
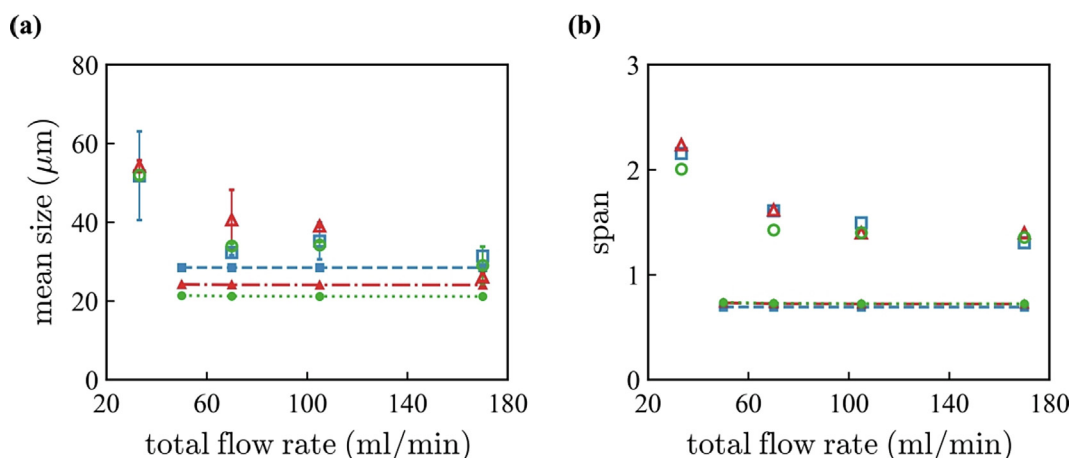
(a)

(b)

Fig. 5. The predictions (lines with filled markers) for the mean secondary particle size and span versus the flow rate by removing the aggregation from the model for $[M^{2+}]$:$[NH_3]$ = "1:0.5" (green circles), "1:1" (red triangles) and "1:2" (blue squares). The metal feed concentration $[M^{2+}]$ is 1 M; Measurements are shown by hollow markers.

measured experimentally. This highlights that the decreasing profile of the mean particle size and span versus the flow rate is mainly due to the aggregation. Moreover, the effect of the aggregation is stronger at low flow rates, which implies that the more intense is turbulence, the lower is aggregation. In other words, turbulence can decrease particle aggregation by altering the aggregation efficiency. It should be mentioned that the predicted particle sizes are still in order of micrometer, even when no particle aggregation is considered in the modelling. On other words, the molecular growth rate obtained by the optimization is higher than expected. Therefore, we believe that it is the combination of the models that predicts the experimentally observed particles sizes, while there are uncertainties around each individual model.

In addition, it is useful to observe the profiles of the mean particle size and span number versus the metal feed concentration, as shown in Fig. 6 for the three $[M^{2+}]:[NH_3]$ ratios and a total flow rate of 70 mL/min. The common trend among the profiles is that the mean particle size shows a minimum as the metal feed concentration increases. The slight decrease of the particle size can be attributed to the fact that a higher feed concentration results in higher levels of supersaturation, which eventually cause more nucleation, and therefore, a smaller mean particle size. However, a further increase of the feed concentration promotes aggregation as the particle number density rises due to the higher nucleation rates, which can also be inferred from the sharp rise in the span number

measured at high concentrations. Likewise, the predictions exhibit the same decreasing-increasing trend in the mean particle size. In addition, good agreement is obtained between the predicted and measured mean particles size, except for the highest metal feed concentration, where an intense effect of aggregation can be observed from both the mean particle size and span number. As far as the span number is concerned, the predictions are lower than the measured values, which, as explained before, can be related to the partial loss of polydispersity due to the plug flow assumption in the simplified model.

Now we turn our attention to the particle morphology. Fig. 7 shows some FESEM images taken from particle samples obtained at three different metal feed concentrations, for a total flow rate of 70 mL/min and $[M^{2+}]:[NH_3]$ ratio of "1:1". The images illustrate how the particles are formed by the smaller structures that are referred to as primary particles. Regarding the shape of primary particles, it can be observed from Fig. 7(a) that, at low concentrations, it is more spherical, while they tend to grow in one preferential direction as the feed concentration increases. In fact, rod-like structures are evident in particles formed at a metal feed concentration of 2 M, see Fig. 7(c).

The mean primary particle size can be estimated from the FESEM images by measuring the dimension of the small structures. This is reported in Fig. 8 for syntheses carried out at three $[M^{2+}]$:$[NH_3]$ ratios with a total flow rate of 70 mL/min. The corresponding
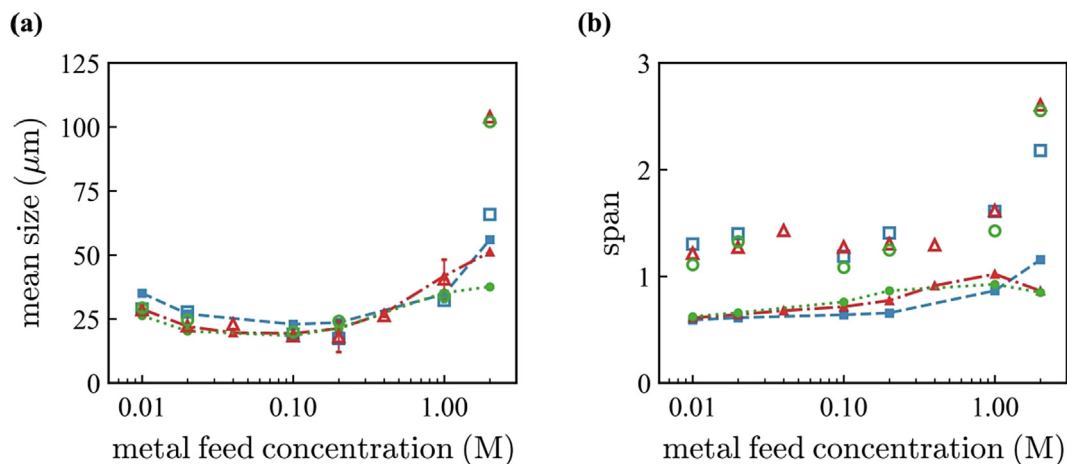
Fig. 6. Measurements (hollow markers) and predictions (lines with filled markers) for the mean secondary particle size and span versus the metal feed concentration at $[M^{2+}]:[NH_3]$ ratio of "1:0.5" (green circles), "1:1" (red triangles) and "1:2" (blue squares). The total flow rate is 70 mL/min.
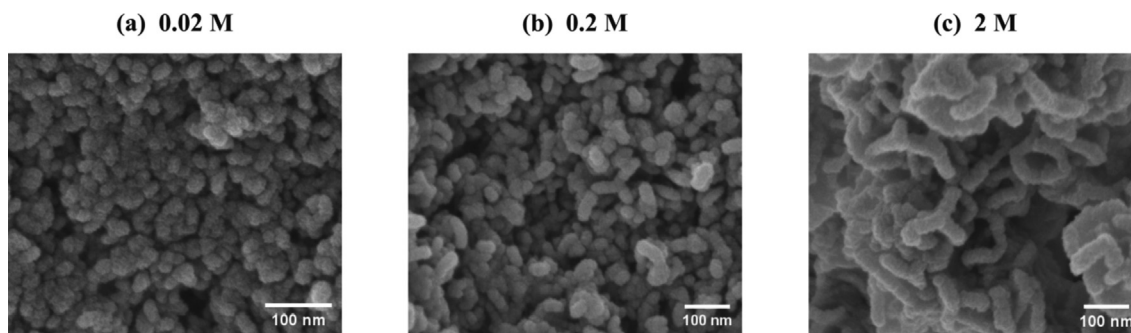

Fig. 7. FESEM images of particles synthesized at three metal feed concentrations. Total flow rate is 70 mL/min and $[M^{2+}]:[NH_3]$ = "1:1".
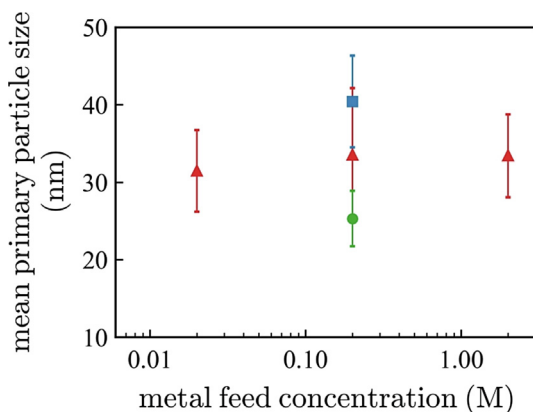

Fig. 8. Mean primary particle size observed in FESEM images versus metal feed concentrations at different $[M^{2+}]:[NH_3]$ ratios of "1:0.5" (green circle), "1:1" (red triangles) and "1:2" (blue square). The total flow rate is 70 mL/min.

FESEM images are reported in Fig. 7 and in Fig. S4 of the Supplementary Material. In the case of two growth directions, e.g., metal feed concentrations of 0.2 and 2 M, the smallest dimension is reported.

As it can be seen from Fig. 8, the mean primary particle size for $[M^{2+}]:[NH_3]$ = 1:1 (red triangles) is around 32 nm with variations within the error bars. It suggests that the metal feed concentration does not have a significant effect on the growth of primary particles in the direction along their smallest dimension. However, it does not mean that the increase of the metal feed concentration

does not influence the primary particles because as mentioned previously, it changes the morphology of primary particles from spherical to rod-like. Instead, comparison between the dimension of particles produced at $[M^{2+}]:[NH_3]$ ratios of "1:0.5" (green circle), "1:1" (red triangles) and "1:2" (blue square) show that the increase of the ammonia concentration favors the growth of the small structures.

Fig. 9 shows the tap density of precipitated particles versus total flow rate for metal feed concentration of 1 M and $[M^{2+}]:[NH_3]$ = 1:1. The measured tap density varies between 1.4 and 1.8 g/cm^3. Excluding the measurement at the lowest total flow
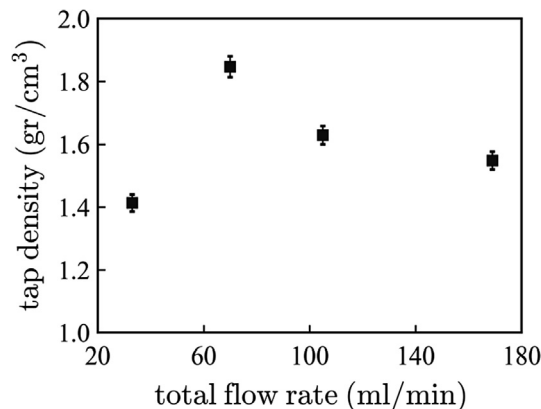

Fig. 9. Effect of the total flow rate on the tap density of precipitated crystals for metal feed concentration of 1 M and $[M^{2+}]:[NH_3]$ = "1:1".

rate, a decreasing trend is evident in Fig. 9. It can be attributed to the decrease of the mean particle size as the flow rate increases (see Fig. 4). In fact, there are reports in the literature that the tap density increases with the particle size (Yang et al., 2012). Instead, at the lowest flow rate, the mixing is not turbulent anymore, which causes a sharp decrease in the tap density of the precipitated particles.

As already mentioned, secondary particles are formed, in the supersaturated solution, by the aggregation of primary particles that undergo molecular growth simultaneously. Primary particles are, in turn, formed by the assembly of smaller building blocks, namely crystallites, produced by simultaneous nucleation and molecular growth. These smaller structures can be partially characterized by XRD. Fig. 10 plots the diffractograms of $Ni_{0.8}Mn_{0.1}Co_{0.1}(OH)_2$ crystals synthesized with different total flow rates for the metal feed concentration of 1 M and $[M^{2+}]:[NH_3]$ = 1:1. Comparison of the diffractograms, for the three highest total flow rates, suggests that the crystallinity of the sample decreases when the flow rate increases, as proven by the fact that the peaks broaden, and their intensity reduces. This behavior can be associated with mixing, that becomes more efficient as the total flow rate increases. In fact, supersaturation increases under faster mixing conditions, leading to higher nucleation rates, resulting in turn in a larger number of nuclei, that then assemble faster, eventually resulting in lower crystallinity.

The diffractograms of particles shown in Fig. 10 are very similar to the diffractogram of $Ni(OH)_2$. In addition, the peaks 28.6° and 54.04° of the diffractogram for pure $Mn(OH)_2$ are not observed in the diffractograms of particles (see Fig. S7 of the Supplementary Material). This implies that Mn^{2+} substitute Ni^{2+} atoms randomly in the $Ni(OH)_2$ lattice, which has been also reported in the literature (Hall et al., 2014; Lee et al., 2004; Xu et al., 2018). The same conclusion can be also extended to Co^{2+}, despite the fact that the

diffractogram of $Co(OH)_2$ is similar to that of $Ni(OH)_2$, which makes it difficult to examine the absence or presence of $Co(OH)_2$. Because, there are reports in the literature that this co-precipitation method results in homogeneous distribution of metals in particles (Huang et al., 2015). In fact, these systems are known as solid solutions since the space group remains the same, in spite of the changes in the unit cell parameters (Hall et al., 2014).

It is known that the crystalline structure of $Ni(OH)_2$ depends on the synthesis condition. For instance, Xu et. al reported that α-Ni $(OH)_2.0.75$ H_2O phase forms predominantly at pH < 11, while the observed patterns at pH > 11 correspond to β–$Ni(OH)_2$ phase (Xu et al., 2018). The patterns of pure β–$Ni(OH)_2$ and α -$Ni(OH)_2.0.75$ H_2O are reported in Fig. 10f and e, respectively. The comparison between the measured patterns with those of pure phases show that at all the investigated total flow rates, the β–$Ni(OH)_2$ structure is the prevailing, or at least the most abundant, phase. This is in agreement with the pH values calculated by the model, since when the feeds are brought into contact the pH is (much) higher than 11 and it decreases as the co-precipitation occurs (see, for instance, Fig. 2). The most intense peak of α -$Ni(OH)_2.0.75$ H_2O phase can be identified in the diffractograms a and d (marked with a star at 2 θ = 11.4° in Fig. 10), and also in the diffractogram of the crystal obtained at different $[M^{2+}]:[NH_3]$ ratios at the highest flow rate (see Fig. S6 of the Supplementary Material). This peak in not observed in patterns b and c (even though small fraction of α-phase may be present, as its peaks are much less intense). In general, the calculated crystallinity of β–$Ni(OH)_2$ is between 60% and 80% for all the flow rates and $[M^{2+}]:[NH_3]$ ratios, see Fig. S5 of the Supplementary Material.

Broadening of the peaks can be also caused by the reduction of the crystallite size; the Scherrer method can be used to estimate it, after correction for the instrumental broadening, by the following formula (Langford & Wilson, 1978):

$$D = \frac{k\lambda}{\beta cos\vartheta} \tag{7}$$

where D is the particles size, k the Scherrer constant, λ the wavelength of the radiation, β the additional broadening in radians and θ the Bragg angle.

Microstrains and structural disorder (incorporation of foreign ions, variable hydration and crystal defects including stacking faults) are responsible for modification of the spectrum, and in particular peak broadening (Hall et al., 2014). The presence of stackings faults in $Ni(OH)_2$ diffractogram results in a selective broadening of the peaks (10l) (Delmas & Tessier, 1997; Ramesh, 2009; Song et al., 2002; Tessier et al., 1999). The peaks (1 0 1) and (1 0 2) are the most influenced ones by stackings faults (Tessier et al., 1999). Therefore, the peaks (0 0 1) and (1 0 0) are used to estimate the crystallite size, even if some effects have been reported also for peak (0 0 1) (Hall et al., 2014), and the corresponding peak is sometimes irregular with appreciable shifts. The calculation steps include fitting the selected peaks with the software OriginPro 2015 (OriginLab Corporation), and then using peak positions and their full width of half-maximum intensity (FWHM) in the X'pert HighScore Scherrer calculator (see Table S1 and Table S2 of the Supplementary Material for peak positions (2θ) and FWHM data). This procedure allows to calculate only the order of magnitude of the crystallite size, and therefore, these results should be treated with care. In Fig. 11a, the mean crystallite size is plotted against $[M^{2+}]:[NH_3]$ ratio for metal feed concentration of 1 M and total flow rate of 169 mL/min. The corresponding XRD patterns are presented in Fig. S6 of the Supplementary Material. Instead, Fig. 11b shows the mean crystallite size versus total flow rate for the metal feed concentration of 1 M and $[M^{2+}]:[NH_3]$ = 1:1. As it can be seen from Fig. 11, the $[M^{2+}]:[NH_3]$ ratio

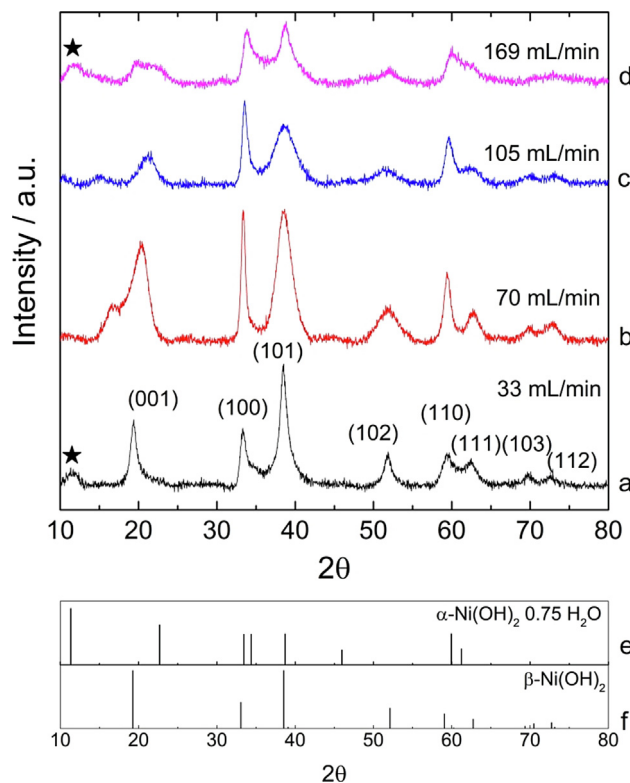Fig. 10. XRD patterns for $Ni_{0.8}Mn_{0.1}Co_{0.1}(OH)_2$ crystals obtained at different total flow rates of 33 (a), 70 (b), 105 (c) and 169 (d) mL/min. The metal feed concentration is 1 M and [M2 +]:[NH3] = "1:1".
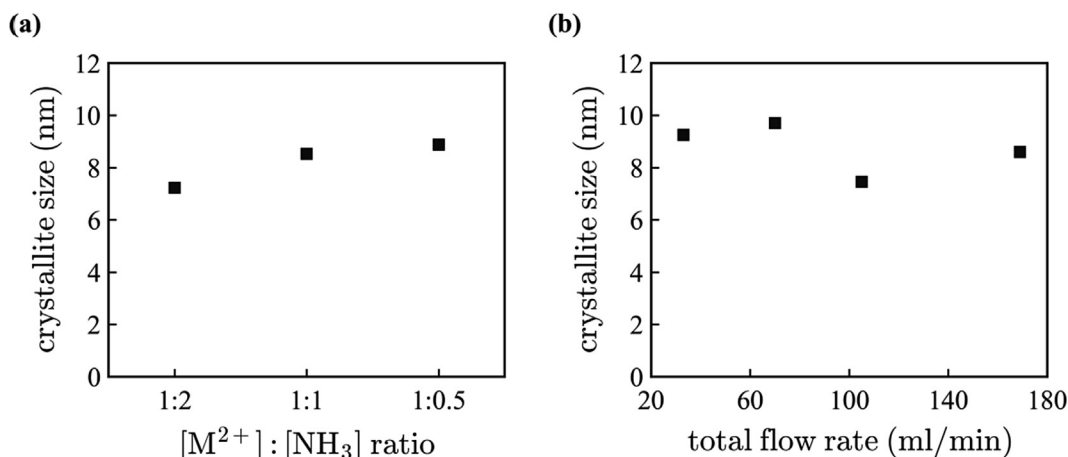
(a)

(b)

Fig. 11. Crystallite size obtained with the Scherrer analysis for metal feed concentration of 1 M. (a) Crystallite size versus $[M^{2+}]$:$[NH_3]$ ratio at total flow rate of 169 mL/min. (b) Crystallite size versus total flow rate for $[M^{2+}]$:$[NH_3]$="1:1".
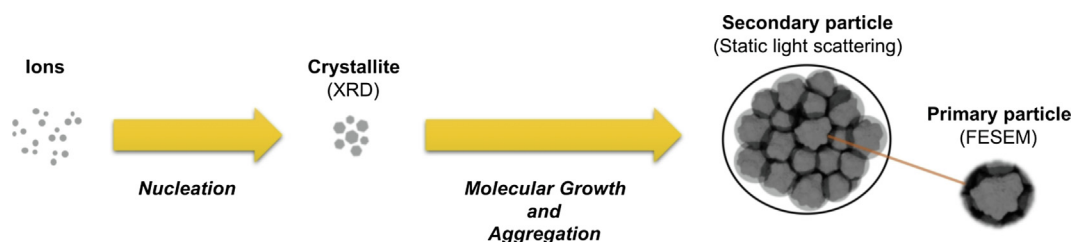

Fig. 12. Sketch of the proposed co-precipitation mechanism and corresponding experimental techniques employed to characterize the particles.

and total flow rate do not have a significant effect on the mean crystallite size, which assumes values below 10 nm.

Full-width of half- maximum intensities have been also reported for the peaks $(1 0 1)$ and $(1 0 2)$ in Table S2 of the Supplementary Material for completeness, but deep investigation of structural characteristics of particles is beyond the scope of this work.

4. Conclusions

The reported experimental observations and the capability of the model (accounting solely for mixing, nucleation, molecular growth, turbulent and Brownian aggregation) to reproduce them allow us to propose a mechanism for the co-precipitation of $Ni_{0.8}$-$Mn_{0.1}Co_{0.1}(OH)_2$. This is depicted in Fig. 12. Let us begin from secondary particles, which are observed in the FESEM images, and their size is measured by static light-scattering. FESEM images illustrate that secondary particles are probably formed by the simultaneous aggregation and growth of smaller primary particles. Aggregation of primary particles is probably caused mainly by turbulent fluctuations. Moreover, the fact that the model well describes the experimentally observed trends supports the hypothesis that (homogeneous) nucleation gives birth to tiny structures, namely the crystallites, that grow and aggregate (mainly by Brownian motions) to form primary particles. FESEM observations also show that the shape of primary particles is spherical or rod-like depending on the feed concentration. Furthermore, their size increases as the concentration of the chelating agent (i.e., ammonia) increases. Finally, the building blocks of the primary particles, i.e., crystallites, can be examined by XRD analyses. According to the observed patterns, it can be concluded that

the crystallite structure resembles that of β–$Ni(OH)_2$, which is attributed to the pH condition at which the co-precipitation occurs. Moreover, it seems that the lattice of $Ni(OH)_2$ remains intact under the presence of Mn and Co, which implies that Mn and Co atoms replace those of Ni randomly.

This groundwork forms the basis for future works to study the effect of precursor morphology on the final electrochemical properties of the active material $LiNi_xCo_yMn_zO_2$. It is worth mentioning that a precise control of precursor characteristics is highly important as it influences the morphological characteristics of the active material, which in turn determine its electrochemical activity.

Author contributions

M. L. Para and M. Alidoost designed the experimental set up, conducted the experimental campaign and analyzed the collected data. They also prepared a first draft of the manuscript. M. Shiea's contribution include developing the modelling framework, performing the simulations, analyzing the results, and writing and revising the manuscript. G. Boccardo and A. Buffo contributed to the design of the experimental campaign and the analysis of the collected data. A. A. Barresi helped in designing the experimental campaign, analyzing the data and correcting the manuscript. D. L. Marchisio contributed with the coordination of the overall research work and contributed to the writing of the manuscript.

Declaration of Competing Interest

The authors declare that they have no known competing financial interests or personal relationships that could have appeared to influence the work reported in this paper.

Acknowledgements

Appendix A. Supplementary material

Supplementary data to this article can be found online at https://doi.org/10.1016/j.ces.2022.117634.

References

Bałdyga, J., Jasińska, M., Orciuch, W., 2003. Barium sulphate agglomeration in a pipe—an experimental study and CFD modeling. Chem. Eng. Technol. 26 (3), 334–340. https://doi.org/10.1002/ceat.200390051.

Barai, P., Feng, Z., Kondo, H., Srinivasan, V., 2019. Multiscale computational model for particle size evolution during coprecipitation of Li-Ion battery cathode precursors. J. Phys. Chem. B 123 (15), 3291–3303. https://doi.org/10.1021/acs.jpcb.8b12004.

Bensaid, S., Deorsola, F.A., Marchisio, D.L., Russo, N., Fino, D., 2014. Flow field simulation and mixing efficiency assessment of the multi-inlet vortex mixer for molybdenum sulfide nanoparticle precipitation. Chem. Eng. J. 238, 66–77. https://doi.org/10.1016/j.cej.2013.09.065.

Bromley, L.A., 1973. Thermodynamic properties of strong electrolytes in aqueous solutions. AIChE J. 19 (2), 313–320. https://doi.org/10.1002/aic.690190216.

Cheng, J.C., Fox, R.O., 2010. Kinetic modeling of nanoprecipitation using CFD coupled with a population balance. Ind. Eng. Chem. Res. 49 (21), 10651–10662. https://doi.org/10.1021/ie100558n.

David, R., Marchal, P., Klein, J.-P., Villermaux, J., 1991. Crystallization and precipitation engineering—III. A discrete formulation of the agglomeration rate of crystals in a crystallization process. Chem. Eng. Sci. 46 (1), 205–213. https://doi.org/10.1016/0009-2509(91)80130-Q.

Delmas, C., Tessier, C., 1997. Stacking faults in the structure of nickel hydroxide: a rationale of its high electrochemical activity. J. Mater. Chem. 7 (8), 1439–1443. https://doi.org/10.1039/a701037k.

Ferri, A., Kumari, N., Peila, R., Barresi, A.A., 2017. Production of menthol-loaded nanoparticles by solvent displacement. Can. J. Chem. Eng. 95 (9), 1690–1706.

Fox, R.O., 1998. On the relationship between Lagrangian micromixing models and computational fluid dynamics. Chem. Eng. Process. Process Intensif. 37 (6), 521–535. https://doi.org/10.1016/S0255-2701(98)00059-2.

Hall, D.S., Lockwood, D.J., Bock, C., MacDougall, B.R., 2014. Nickel hydroxides and related materials: a review of their structures, synthesis and properties. Proc. R. Soc. A 471, 1024–1027. https://doi.org/10.1098/rspa.2014.0792.

Huang, Y., Wang, Z.X., Li, X.H., Guo, H.J., Wang, J.X., 2015. Synthesis of $Ni_{0.8}Co_{0.1}Mn_{0.1}(OH)_2$ precursor and electrochemical performance of $LiNi_{0.8}Co_{0.1}Mn_{0.1}O_2$ cathode material for lithium batteries. Trans. Nonferrous Metals Soc. China (English Edition) 25 (7), 2253–2259. https://doi.org/10.1016/S1003-6326(15)63838-9.

Isaacson, E., Keller, H.B., 1966. Analysis of Numerical Methods. Wiley, New York.

Kosova, N.V., Devyatkina, E.T., Kaichev, V.V., 2007. Mixed layered Ni-Mn-Co hydroxides: crystal structure, electronic state of ions, and thermal decomposition. J. Power Sources 174 (2), 735–740. https://doi.org/10.1016/j.jpowsour.2007.06.109.

Langford, J.I., Wilson, A.J.C., 1978. Seherrer after sixty years: a survey and some new results in the determination of crystallite size. J. Appl. Cryst. 11, 102–113.

Lee, M.-H., Kang, Y.-J., Myung, S.-T., Sun, Y.-K., 2004. Synthetic optimization of Li $[Ni_{1/3}Co_{1/3}Mn_{1/3}]O_2$ via co-precipitation. Electrochim. Acta 50 (4), 939–948. https://doi.org/10.1016/j.electacta.2004.07.038.

Lince, F., Marchisio, D., Barresi, A., 2011. A comparative study for nanoparticle production with passive mixers via solvent-displacement: use of CFD models for optimization and design. Chem. Eng. Process. Process Intensif. 50 (4), 356–368. https://doi.org/10.1016/j.cep.2011.02.015.

Liu, Y., Fox, R.O., 2006. CFD predictions for chemical processing in a confined impinging-jets reactor. AIChE J. 52 (2), 731–744. https://doi.org/10.1002/aic.10633.

Liu, Y., Cheng, C., Liu, Y., Prud'homme, R.K., Fox, R.O., 2008. Mixing in a multi-inlet vortex mixer (MIVM) for flash nano-precipitation. Chem. Eng. Sci. 63 (11), 2829–2842. https://doi.org/10.1016/j.ces.2007.10.020.

Marchisio, D.L., Barresi, A.A., Fox, R.O., 2001. Simulation of turbulent precipitation in a semi-batch Taylor-Couette reactor using CFD. AIChE J. 47 (3), 664–676. https://doi.org/10.1002/aic.690470314.

Marchisio, D.L., Barresi, A.A., Garbero, M., 2002. Nucleation, growth, and agglomeration in barium sulfate turbulent precipitation. AIChE J. 48 (9), 2039–2050. https://doi.org/10.1002/aic.690480917.

Marchisio, D., Omegna, F., Barresi, A.A., Bowen, P., 2008. Effect of mixing and other operating parameters in sol- gel processes. Ind. Eng. Chem. Res. 47 (19), 7202–7210. https://doi.org/10.1021/ie800217b.

Marchisio, D.L., Pikturna, J.T., Fox, R.O., Vigil, R.D., Barresi, A.A., 2003. Quadrature method of moments for population-balance equations. AIChE J. 49 (5), 1266–1276. https://doi.org/10.1002/aic.690490517.

Mersmann, A., 2001. Physical and chemical properties of crystalline systems. In: Crystallization Technology Handbook. second ed. Marcel Dekker Inc, New York, pp. 1–44.

Mersmann, A., Braun, B., 2001. Agglomeration. In: Crystallization Technology Handbook. CRC Press, pp. 249–298.

Ramesh, T.N., 2009. Crystallite size effects in stacking faulted nickel hydroxide and its electrochemical behaviour. Mater. Chem. Phys. 114 (2–3), 618–623. https://doi.org/10.1016/j.matchemphys.2008.10.017.

Saffman, P.G.F., Turner, J.S., 1956. On the collision of drops in turbulent clouds. J. Fluid Mech. 1 (1), 16–30. https://doi.org/10.1017/S0022112056000020.

Shiea, M., Buffo, A., Vanni, M., Marchisio, D., 2020. Numerical methods for the solution of population balance equations coupled with computational fluid dynamics. Annu. Rev. Chem. Biomol. Eng. 11 (1), 339–366. https://doi.org/10.1146/annurev-chembioeng-092319-075814.

Song, Q., Tang, Z., Guo, H., Chan, S.L.I., 2002. Structural characteristics of nickel hydroxide synthesized by a chemical precipitation route under different pH values. J. Power Sources 112 (2), 428–434. https://doi.org/10.1016/S0378-7753(02)00396-8.

Tessier, C., Haumesser, P.H., Bernard, P., Delmas, C., 1999. The structure of $Ni(OH)_2$: from the ideal material to the electrochemically active one. J. Electrochem. Soc. 146 (6), 2059–2067. https://doi.org/10.1149/1.1391892.

van Bommel, A., Dahn, J.R., 2009. Analysis of the growth mechanism of coprecipitated spherical and dense nickel, manganese, and cobalt-containing hydroxides in the presence of aqueous ammonia. Chem. Mater. 21 (8), 1500–1503. https://doi.org/10.1021/cm803144d.

Volmer, M., Weber, A., 1926. Keimbildung in übersättigten Gebilden. Z. Phys. Chem. 119 (1), 277–301. https://doi.org/10.1515/zpch-1926-11927.

Xu, L., Zhou, F., Kong, J., Chen, Z., Chen, K., 2018. Synthesis of $Li(Ni_{0.6}Co_{0.2}Mn_{0.2})O_2$ with sodium DL-lactate as an eco-friendly chelating agent and its electrochemical performances for lithium-ion batteries. Ionics 24 (8), 2261–2273. https://doi.org/10.1007/s11581-017-2363-8.

Yang, S., Wang, X., Yang, X., Liu, Z., Wei, Q., Shu, H., 2012. High tap density spherical $Li[Ni_{0.5}Mn_{0.3}Co_{0.2}]O_2$ cathode material synthesized via continuous hydroxide coprecipitation method for advanced lithium-ion batteries. Int. J. Electrochem. 2012, 1–9. https://doi.org/10.1155/2012/323560.

Zhou, F., Zhao, X., Van Bommel, A., Rowe, A.W., Dahn, J.R., 2010. Coprecipitation synthesis of $Ni_xMn_{1-x}(OH)_2$ mixed hydroxides. Chem. Mater. 22 (3), 1015–1021. https://doi.org/10.1021/cm9018309.